

Best-Fit Ellipsoids of Atom-Probe Tomographic Data to Study Coalescence of γ' (L1₂) Precipitates in Ni-Al-Cr

Richard A. Karnesky^{a,*} Chantal K. Sudbrack^a
David N. Seidman^{a,b}

^a*Department of Materials Science and Engineering, Northwestern University,
Evanston, IL 60208-3108, USA*

^b*Northwestern University Center for Atom-Probe Tomography (NUCAPT),
Evanston, IL 60208-3108, USA*

Abstract

An algorithm is presented to fit precipitates in atom probe tomographic data sets as equivalent ellipsoids. Unlike previous techniques, which measure only the radius of gyration, these ellipsoids retain the moments of inertia and principle axes of the original precipitate, preserving crystallographic orientational information. The algorithm is applied to study interconnected γ' -precipitates (L1₂) in the γ -matrix (FCC) of a Ni-Al-Cr alloy. The precipitates are found to coagulate along $\langle 110 \rangle$ -type directions.

Key words: Best-fit ellipsoid, Atom-probe tomography, Coarsening, Nickel alloys

* Corresponding author.

Email address: karnesky@northwestern.edu (Richard A. Karnesky).

URL: <http://arc.nucapt.northwestern.edu/> (Richard A. Karnesky).

1 One of the principle challenges that analyzing three-dimensional atom-probe
2 tomographic (APT) results poses is the amount of raw data that the instru-
3 ments are now able to collect [1,2]; we have collected continuous data sets as
4 large as 2.1×10^8 properly ranged atoms from a single specimen. It is neces-
5 sary to extract information about spatial and compositional measures, such
6 as precipitate size from these data sets. A common method to measure the
7 size of precipitates is to calculate a single radius of gyration (or, from this, the
8 Guinier radius) [3,4]. While this technique works well for equiaxed, spheroidal
9 precipitates [5,6], many alloy systems investigated by APT have non-spherical
10 features [7,8,9,10,11,12,13,14,15]. Improperly reconstructed data sets, which
11 have preferential evaporation or local-magnification effects, may also exhibit
12 non-spherical features [16]. Techniques that measure the angular eccentricity
13 of features can be used to quantify the accuracy of a reconstruction. The radius
14 of gyration technique does not, however, retain three-dimensional information
15 concerning precipitate orientation.

16 In this article, a more general alternative to the radius of gyration is presented
17 and applied. Best-fit ellipsoids have equivalent centroids, moments of inertia,
18 and principle axes for arbitrarily shaped precipitates. The crystallographic
19 orientations of the resulting ellipsoids are then used to study the coagulation-
20 coalescence coarsening mechanism in a Ni-Al-Cr alloy, which occurs when
21 the γ' -precipitate number density is large ($> 10^{24} \text{ m}^{-3}$) and the edge-to-edge
22 distance between adjacent γ' -precipitates is small ($< 2 \text{ nm}$) [17,18].

23 In lattice kinetic Monte Carlo simulations, a coagulation-coalescence coarsen-
24 ing mechanism is reported [18]. This mechanism is caused by non-equilibrium
25 overlapping diffusion fields, which originate from the long-range vacancy-solute
26 binding energies and a small mean edge-to-edge interprecipitate distance. The
27 non-equilibrium concentration profiles observed at the γ' -precipitate/ γ -matrix
28 interfaces lead to a higher interfacial free energy than for fully equilibrated
29 γ' -precipitates. The excess free energy of the region of overlapping concen-
30 tration profiles (“diffuse neck”) can decrease by changing the concentration
31 thereof into a well-formed neck [18]. Phase-field simulations find that the rate
32 of γ' -precipitate coalescence is increased when the γ/γ' -interfacial width is
33 increased artificially, thereby increasing the overlapping diffusion fields [19].
34 While nanometer-sized coagulated γ' -precipitates might have been observed
35 experimentally, past studies only commented on whether precipitates appeared
36 to be non-equiaxed [20,21,22], necked [23,24], or chemically ordered [17]. They
37 did not explore the crystallographic orientation for precipitate coagulation.

38 A Ni-5.2 Al-14.2 Cr (at.%) alloy was melted under an Ar atmosphere and
39 chill cast. Its chemical composition was verified by inductively coupled plasma
40 spectroscopy. The alloy was homogenized for 24 h at 1300°C, which resulted
41 in coarse grains (0.5–2 mm diameter). After homogenization, the alloy was
42 annealed at 900°C (γ -phase field) and water quenched to ambient tempera-

43 ture. The solutionized alloy was sectioned and aged for 4 h at 600°C and then
 44 quenched. This treatment leads to the greatest percentage of γ' -precipitates
 45 that are interconnected by necks ($30 \pm 4\%$) [17]. The specimens were cut,
 46 ground, and then electropolished into APT tips. Three separate APT runs of
 47 ca. 3×10^6 atoms were collected on a first-generation 3-D APT [25,26] at a
 48 specimen temperature of 40.0 ± 0.3 K, a pulse fraction of 19%, and a pulse
 49 repetition rate of 1.5 kHz. The computer programs IVAS (Imago Scientific In-
 50 struments) and ADAM [27] were used to analyze APT data. The γ/γ' interface
 51 is delineated using a 9 at.% Al isoconcentration surface [28] and the atoms
 52 contained within the γ' -surface were exported and segmented into individual
 53 γ' -precipitates by a modified envelope algorithm [3,4,29,30].

54 The γ' -precipitates are divided into three classes: (i) single γ' -precipitates (un-
 55 coagulated, without a concave neck) that are not cut by the surface of the ana-
 56 lyzed volume; (ii) two or more coalesced γ' -precipitates that are interconnected
 57 by a concave neck; (iii) γ' -precipitates cut by the analysis volume boundary.
 58 Class (i) accounts for 42% of γ' -precipitates analyzed, class (ii) accounts for
 59 28% of the γ' -precipitates analyzed, and only 12% of them are formations of
 60 more than two γ' -precipitates (the largest of which is made up of five dis-
 61 tinguishable γ' -precipitates). The best-fit ellipsoid method yields quantitative
 62 results for all three classes; particularly class (ii), which is important for under-
 63 standing the coagulation-coalescence mechanism of γ' -precipitate coarsening.

64 [Fig. 1 about here.]

65 A schematic that explains the fitting of an equivalent ellipsoid to atoms of
 66 coagulated and coalesced precipitates is presented in Fig. 1. For a reference
 67 space defined by Cartesian axes X_1 , X_2 , X_3 (typically the analysis direction
 68 and the two orthogonal principle directions of the area detector), the major
 69 and minor axes of the best-fit ellipsoid of a precipitate containing N atoms
 70 are determined directly from its eigenvalues (λ_1 , λ_2 , λ_3), also referred to as
 71 the principle axes [31]. The principle axes are segments along the transformed
 72 Cartesian X'_1 , X'_2 , and X'_3 axes and are obtained from the diagonalization of
 73 the characteristic length matrix, L (also known as the inertia tensor). This
 74 diagonalization is obtained by a Jacobian transformation [32] of a symmetric
 75 second-rank tensor, as follows:

$$L = \begin{bmatrix} l_{11} & l_{12} & l_{13} \\ l_{12} & l_{22} & l_{23} \\ l_{13} & l_{23} & l_{33} \end{bmatrix} \xrightarrow{\text{transform}} \begin{bmatrix} \lambda_1 & 0 & 0 \\ 0 & \lambda_2 & 0 \\ 0 & 0 & \lambda_3 \end{bmatrix}; \quad (1)$$

76 where the characteristic lengths, l_{jk} , are calculated from the positions of i^{th}
 77 atom in the reference space ($x_1(i)$, $x_2(i)$, and $x_3(i)$), relative to a precipitate's

78 center of mass ($x_1(com)$, $x_2(com)$, and, $x_3(com)$), averaged over N atoms,
 79 employing:

$$l_{kk} = \frac{1}{N} \sum_i \left(\sum_{j \neq k} (x_j(i) - x_j(com))^2 \right) \quad (2)$$

$$l_{jk} = -\frac{1}{N} \sum_i ((x_j(i) - x_j(com))(x_k(i) - x_k(com))) \quad \text{for } j \neq k \quad (3)$$

80 The diagonalization of the L matrix follows a procedure outlined in Ref. [32].
 81 The transformation matrix used for this diagonalization yields the orientation
 82 of the ellipsoid with respect to the reference state. Defining $\lambda_1 \geq \lambda_2 \geq \lambda_3$, the
 83 semi-axes (S_i) of the best-fit ellipsoid are given by:

$$S_i = \sqrt{\frac{5}{2} (\lambda_j + \lambda_k - \lambda_i)} \quad \text{for } j \neq k; \quad (4)$$

84 where $S_3 \geq S_2 \geq S_1$ are the major semi-axis and two minor semi-axes, respec-
 85 tively.

86 [Fig. 2 about here.]

87 Figure 2 shows a reconstruction of one APT data set where ellipsoids have been
 88 fit to interconnected γ' -precipitates. As is seen, the best-fit ellipsoid retains 3-
 89 D size and crystallographic orientation information that is jettisoned by other
 90 techniques [3,4].

91 Single γ' -precipitates that are not cut by the analysis volume have aspect
 92 ratios of $\frac{S_3}{S_2} = 1.5 \pm 0.5$ and $\frac{S_2}{S_1} = 1.3 \pm 0.2$. The closeness of these values to
 93 unity is consistent with equiaxed, uncoagulated precipitates.

94 Coalesced γ' -precipitates that are interconnected by necks have aspect ratios
 95 of $\frac{S_3}{S_2} = 2.9 \pm 0.9$ and $\frac{S_2}{S_1} = 1.3 \pm 0.3$. The ratio for $\frac{S_3}{S_2}$ is about twice the
 96 same ratio for uncoagulated precipitates, but $\frac{S_2}{S_1}$ is about the same for the two
 97 classes. This demonstrates that a majority of these consist of two equiaxed
 98 γ' -precipitates that have coagulated and undergone coalescence.

99 Precipitates that are cut by the edge of the analysis volume can serve as a check
 100 of the best-fit ellipsoid method. These have $\frac{S_3}{S_2} = 2.2 \pm 0.8$ and $\frac{S_2}{S_1} = 1.4 \pm 0.4$
 101 because the majority are equiaxed, uncoagulated γ' -precipitates that are, on
 102 average, cut in two by the analysis boundary. Sampling bias by coagulated

103 γ' -precipitates is small, as they make up a minority of precipitates and many
104 can be isolated (if their concave necks are in the analysis volume).

105 [Fig. 3 about here.]

106 It is useful to relate the axes of the analysis volume with specific crystallo-
107 graphic directions to study the orientation of γ' -precipitate coagulation. The
108 analysis direction, which was chosen near the 002 crystallographic pole, pro-
109 vides us with the [001] direction. The [010] and [100] directions can be de-
110 duced from a Field-Ion Microscope (FIM) image (Fig. 3) [33] to within 1–4°.
111 FIM micrographs also demonstrate that local magnification effects are negli-
112 gible in this alloy, which is consistent with the small lattice parameter misfit,
113 $\delta = 0.0006 \pm 0.0004$ [17].

114 [Fig. 4 about here.]

115 The rotation matrix used in the best-fit ellipsoid method yields the Bunge
116 Euler angles [34] for the major principle axis of the γ' -precipitate with re-
117 spect to this crystallographically-resolved reference system. From these, an
118 inverse pole figure (Fig. 4) shows the orientations of γ' -precipitates that are
119 the result of the coagulation-coalescence coarsening. There is a preference for
120 coagulation along the $\langle 110 \rangle$ -type directions. 30% of the coalesced precipitates
121 are within 10° and 71% are within 15° of $\langle 110 \rangle$ -type directions. In the FCC
122 structure of the γ -matrix, $\langle 110 \rangle$ is the fastest diffusion path for solute clus-
123 ters, and is therefore consistent with the model presented in Ref. [18]. Some
124 γ' -precipitates coagulated along $\langle 100 \rangle$, which is the next-fastest diffusion path
125 and none coagulated along $\langle 111 \rangle$, which is a slower path.

126 No crystallographic orientational preference was found for single, uncoagu-
127 lated γ' -precipitates. This supports, once more, the equiaxed nature of γ' -
128 precipitates and the proper reconstruction approach (with negligible local
129 magnification) for analyzing the raw APT data. The γ' -precipitates that are
130 cut by the analysis boundary show a preference for the [100] direction, as that
131 direction makes up the majority of the analysis frustum’s surface.

132 The measurement of size and orientation of non-spheroidal precipitates in APT
133 data requires more spatial information to be preserved than for the commonly
134 used methods currently reported to date. We have demonstrated that the
135 best-fit ellipsoid technique preserves the center of gravity, moment of inertia,
136 and principle axes of any precipitate. The technique is applied to specific re-
137 sults for a Ni-Al-Cr alloy with both uncoagulated equiaxed γ' -precipitates and
138 nonequiaxed lobed precipitates that formed through a coagulation-coalescence
139 coarsening mechanism.

140 Acknowledgements

This research is supported by the National Science Foundation, Division of Materials Research, under contract DMR-0241928. RAK received partial support from a Walter P. Murphy (WPM) Fellowship and the US Department of Energy (DE-FG02-98ER45721). CKS received partial support from an NSF graduate research fellowship, a WPM Fellowship, and a Northwestern University terminal year fellowship. We thank Imago Scientific Instruments and Dr. M. K. Miller for permitting RAK to modify the source code for ENVELOPE, and Dr. D. Mainprice for his inverse pole figure software, IPF2K. Prof. D. C. Dunand, Dr. Z. Mao, and Dr. G. Martin are thanked for discussions.

141 References

- 142 [1] T. F. Kelly, M. K. Miller, Atom probe tomography, Review of Scientific
143 Instruments 78 (2007) 031101:1–20.
- 144 [2] D. N. Seidman, Three-dimensional atom-probe tomography: Advances and
145 applications, Annual Review of Materials Research 37 (2007) 127–158.
- 146 [3] M. K. Miller, Atom Probe Tomography: Analysis at the Atomic Level,
147 Kluwer Academic/Plenum, New York, 2000.
- 148 [4] M. K. Miller, E. A. Kenik, Atom probe tomography: A technique for
149 nanoscale characterization, Microscopy and Microanalysis 10 (2004) 336–341.
- 150 [5] M. K. Miller, B. D. Wirth, G. R. Odette, Precipitation in neutron-irradiated
151 Fe-Cu and Fe-Cu-Mn model alloys: a comparison of APT and SANS data,
152 Materials Science and Engineering A 353 (2003) 133–139.
- 153 [6] R. P. Kolli, D. N. Seidman, Comparison of compositional and morphological
154 atom-probe tomography analyses for a multicomponent Fe-Cu steel,
155 Microscopy & Microanalysis Submitted,.
- 156 [7] F. Soisson, A. Barbu, G. Martin, Monte Carlo simulations of copper
157 precipitation in dilute iron-copper alloys during thermal ageing and under
158 electron irradiation, Acta Materialia 44 (1996) 3789–3800.
- 159 [8] E. Cadel, D. Lemarchand, S. Chambrelaud, D. Blavette, Atom probe
160 tomography investigation of the microstructure of superalloys N18, Acta
161 Materialia 50 (2002) 957–966.
- 162 [9] A. Heinrich, T. Al-Kassab, R. Kirchheim, Investigation of the early stages of
163 decomposition of Cu-0.7at.% Fe with the tomographic atom probe, Materials
164 Science and Engineering A 353 (2003) 92–98.

- 165 [10] D. Wolde-Giorgis, T. Al-Kassab, R. Kirchheim, Nucleation and growth in Cu-
166 0.7at.% Ti as studied with the tomographic atom probe, *Materials Science*
167 *and Engineering A* A353 (2003) 152–157.
- 168 [11] M. Dumont, W. Lefebvre, B. Doisneau-Cottignies, A. Deschamps,
169 Characterisation of the composition and volume fraction of η' and η
170 precipitates in an Al-Zn-Mg alloy by a combination of atom probe, small-
171 angle X-ray scattering and transmission electron microscopy, *Acta Materialia*
172 53 (2005) 2881–2892.
- 173 [12] D. Isheim, G. Hsieh, R. D. Noebe, D. N. Seidman, Nanostructural temporal
174 evolution and solute partitioning in model Ni-based superalloys containing
175 ruthenium, rhenium, and tungsten, in: J. M. Howe, D. E. Laughlin, J. K.
176 Lee, D. J. Srolovitz, U. Dahmen, W. A. Soffa (Eds.), *Solid-Solid Phase*
177 *Transformations in Inorganic Materials*, Vol. 1, TMS, Warrendale, PA, 2005,
178 pp. 309–314.
179 URL <http://nucapt.northwestern.edu/refbase/show.php?record=187>
- 180 [13] S. D. Erlach, H. Leitner, M. Bischof, H. Clemens, F. Danoix, D. Lemarchand,
181 I. Siller, Comparison of NiAl precipitation in a medium carbon secondary
182 hardening steel and C-free PH13-8 maraging steel, *Materials Science and*
183 *Engineering: A* 429 (2006) 96–106.
- 184 [14] E. V. Pereloma, I. B. Timokhina, K. F. Russell, M. K. Miller,
185 Characterization of clusters and ultrafine precipitates in Nb-containing C-
186 Mn-Si steels, *Scripta Materialia* 54 (2006) 471–476.
- 187 [15] A. Andersson, K. Stiller, M. Hättestrand, Comparison of early stages of
188 precipitation in Mo-rich and Mo-poor maraging stainless steels, *Surface and*
189 *Interface Analysis* 39 (2007) 195–200.
- 190 [16] D. Blavette, F. Vurpillot, P. Pareige, A. Menand, A model accounting for
191 spatial overlaps in 3D atom-probe microscopy, *Ultramicroscopy* 89 (2001)
192 145–153.
- 193 [17] C. K. Sudbrack, K. E. Yoon, R. D. Noebe, D. N. Seidman, Temporal
194 evolution of the nanostructure and phase compositions in a model Ni-Al-Cr
195 alloy, *Acta Materialia* 54 (2006) 3199–3210.
- 196 [18] Z. Mao, C. K. Sudbrack, K. E. Yoon, G. Martin, D. N. Seidman, The
197 mechanism of morphogenesis in a phase separating concentrated multi-
198 component alloy, *Nature Materials* 6 (2007) 210–216.
- 199 [19] J. Z. Zhu, T. Wang, A. J. Ardell, S. H. Zhou, Z. K. Liu, L. Q. Chen, Three-
200 dimensional phase-field simulations of coarsening kinetics of γ' particles in
201 binary Ni-Al alloys, *Acta Materialia* 52 (2004) 2837–2845.
- 202 [20] R. E. Beddoe, P. Haasen, G. Kostorz, Early stages of decomposition in Ni-
203 Al single crystals studied by small-angle neutron scattering, in: P. Haasen,
204 V. Gerold, R. Wagner, M. F. Ashby (Eds.), *Decomposition of Alloys:*
205 *The Early Stages*, Vol. 2 of *Acta-Scripta Metallurgica Proceedings Series*,
206 Pergamon, Oxford, 1984, pp. 233–238.

- 207 [21] C. Schmuck, F. Danoix, P. Caron, A. Hauet, D. Blavette, Atomic scale
208 investigation of ordering and precipitation processes in a model Ni-Cr-Al
209 alloy, *Applied Surface Science* 94–95 (1996) 273–279.
- 210 [22] C. K. Sudbrack, K. E. Yoon, R. D. Noebe, D. N. Seidman, The temporal
211 evolution of the nanostructure of a model Ni-Al-Cr superalloy, *TMS Letters* 1
212 (2004) 25–26.
213 URL <http://nucapt.northwestern.edu/refbase/show.php?record=199>
- 214 [23] C. K. Sudbrack, R. D. Noebe, D. N. Seidman, Temporal evolution of sub-
215 nanometer compositional profiles across the γ/γ' interface in a model Ni-
216 Al-Cr superalloy, in: J. M. Howe, D. E. Laughlin, J. K. Lee, D. J. Srolovitz,
217 U. Dahmen, W. A. Soffa (Eds.), *Solid-Solid Phase Transformations in*
218 *Inorganic Materials*, Vol. 2, TMS, Warrendale, PA, 2005, pp. 543–548.
219 URL <http://nucapt.northwestern.edu/refbase/show.php?record=180>
- 220 [24] C. K. Sudbrack, R. D. Noebe, D. N. Seidman, Compositional pathways and
221 capillary effects during isothermal precipitation in a nondilute Ni-Al-Cr alloy,
222 *Acta Materialia* 55 (2007) 119–130.
- 223 [25] D. Blavette, B. Deconihout, A. Bostel, J. M. Sarrau, M. Bouet, A. Menand,
224 The tomographic atom probe: A quantitative three-dimensional
225 nanoanalytical instrument on an atomic scale, *Review of Scientific*
226 *Instruments* 64 (1993) 2911–2919.
- 227 [26] A. Cerezo, T. J. Godfrey, S. J. Sijbrandij, G. D. W. Smith, P. J. Warren,
228 Performance of an energy-compensated three-dimensional atom probe,
229 *Review of Scientific Instruments* 69 (1998) 49–58.
- 230 [27] O. Hellman, J. Vandenbroucke, J. Blatz du Rivage, D. N. Seidman,
231 Application software for data analysis for three-dimensional atom probe
232 microscopy, *Materials Science and Engineering A* 327 (2002) 29–33.
- 233 [28] O. C. Hellman, J. Blatz du Rivage, D. N. Seidman, Efficient sampling for
234 three-dimensional atom probe microscopy data, *Ultramicroscopy* 95 (2003)
235 199–205.
- 236 [29] J. M. Hyde, C. A. English, An analysis of the structure of irradiation
237 Cu-enriched clusters in low and high nickel welds, in: G. E. Lucas,
238 L. Snead, M. A. Kirk, R. G. Ellman (Eds.), *Microstructural Processes in*
239 *Irradiated Materials–2000*, Vol. 650 of *Materials Research Society Symposia*
240 *Proceedings*, Materials Research Society, Warrendale, PA, 2001, pp. R.6.6.1–
241 12.
- 242 [30] E. A. Marquis, Microstructural evolution and strengthening mechanisms in
243 Al-Sc and Al-Mg-Sc alloys, Ph.D. thesis, Northwestern University (2002).
244 URL <http://nucapt.northwestern.edu/refbase/show.php?record=151>
- 245 [31] J. F. Nye, *Physical Properties of Crystals: Their Representation by Tensors*
246 *and Matrices*, Oxford University Press, Oxford, 1985.

- 247 [32] W. H. Press, S. A. Teukolsky, W. T. Vetterling, B. P. Flannery, Numerical
248 Recipes: The Art of Scientific Computing, 1st Edition, Cambridge University
249 Press, Cambridge, 1986.
- 250 [33] K. M. Bowkett, D. A. Smith, Field-Ion Microscopy, North-Holland,
251 Amsterdam, 1970.
- 252 [34] H. J. Bunge, Texture Analysis in Materials Science: Mathematical Methods,
253 Butterworths, Boston, 1982.

254 **List of Figures**

- 255 1 The best-fit ellipsoid of a precipitate is determined in three
256 steps: (i) for a reference set of axes (X_1 , X_2 , and X_3), identify
257 the x_1 , x_2 , x_3 coordinates of all atoms in a precipitate and
258 its center of mass to obtain a moment of inertia tensor
259 (L) (Eqs. 1–3); (ii) the orientation of the principle axes
260 (X'_1 , X'_2 , and X'_3) of the ellipsoid axes construct a Jacobian
261 transformation matrix that will diagonalize L . (iii) the lengths
262 of the major and minor semi-axes of the best-fit ellipsoid are
263 found from the eigenvalues of the transformed matrix. (Eq. 4). 11
- 264 2 A representative data set for a Ni-5.2 Al-14.2 Cr (at.%)
265 alloy, whose thermal history is discussed in the text. The
266 coloring scheme matches that of Fig. 1, with Ni atoms in
267 green, Al atoms in red, and Cr atoms in blue. The atoms in
268 the γ -matrix (FCC) are omitted for clarity. The gold colored
269 best-fit ellipsoids indicate those $\gamma'(L1_2)$ precipitates that are
270 interconnected by necks. 12
- 271 3 An FIM image, centered on the 002 pole, taken before APT
272 analysis. The small square denotes the area and orientation
273 for the data set in Fig. 1. The larger square connects the 113
274 family of poles and the edges of this square give the [010] and
275 [100] directions. 13
- 276 4 An inverse pole figure for all interconnected γ' ($L1_2$)
277 precipitates in this study, presented in the standard
278 stereographic triangle. There is a preference for coagulation
279 along and close to $\langle 110 \rangle$ -type directions, which is consistent
280 with a diffusion controlled mechanism for coagulation. 14

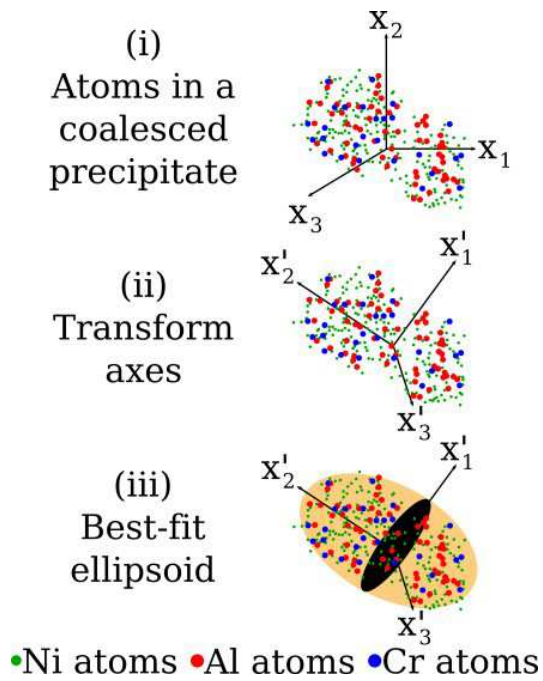


Fig. 1. The best-fit ellipsoid of a precipitate is determined in three steps: (i) for a reference set of axes (X_1 , X_2 , and X_3), identify the x_1 , x_2 , x_3 coordinates of all atoms in a precipitate and its center of mass to obtain a moment of inertia tensor (L) (Eqs. 1–3); (ii) the orientation of the principle axes (X'_1 , X'_2 , and X'_3) of the ellipsoid axes construct a Jacobian transformation matrix that will diagonalize L . (iii) the lengths of the major and minor semi-axes of the best-fit ellipsoid are found from the eigenvalues of the transformed matrix. (Eq. 4).

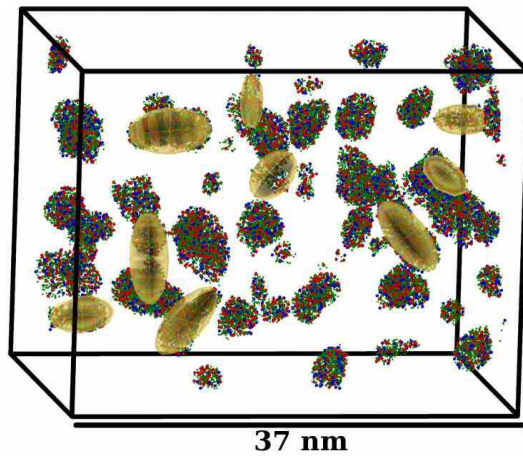


Fig. 2. A representative data set for a Ni-5.2 Al-14.2 Cr (at.%) alloy, whose thermal history is discussed in the text. The coloring scheme matches that of Fig. 1, with Ni atoms in green, Al atoms in red, and Cr atoms in blue. The atoms in the γ -matrix (FCC) are omitted for clarity. The gold colored best-fit ellipsoids indicate those γ' (L₁₂) precipitates that are interconnected by necks.

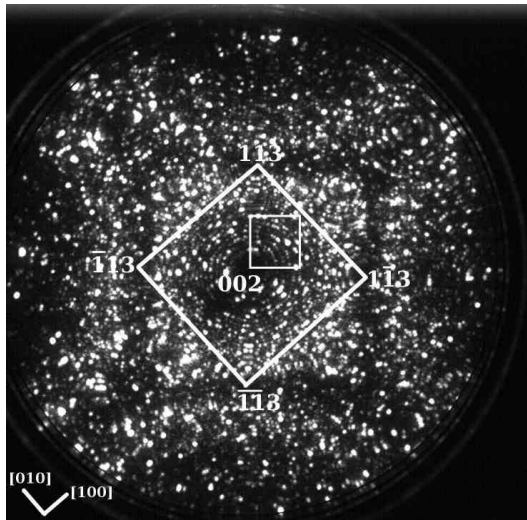


Fig. 3. An FIM image, centered on the 002 pole, taken before APT analysis. The small square denotes the area and orientation for the data set in Fig. 1. The larger square connects the 113 family of poles and the edges of this square give the [010] and [100] directions.

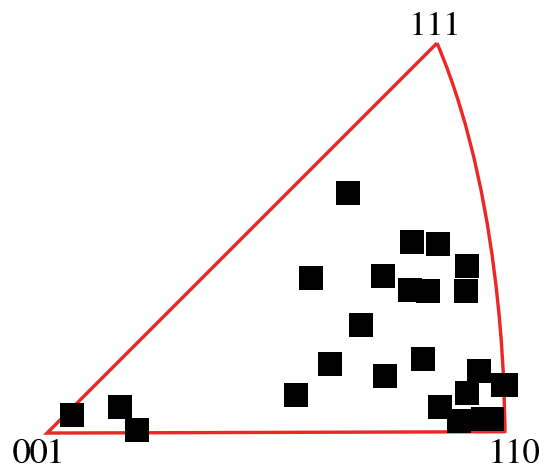


Fig. 4. An inverse pole figure for all interconnected γ' ($L1_2$) precipitates in this study, presented in the standard stereographic triangle. There is a preference for coagulation along and close to $\langle 110 \rangle$ -type directions, which is consistent with a diffusion controlled mechanism for coagulation.